Quantitative characterization of magnetic separators: Comparison of systems with and without integrated microfluidic mixers

**Torsten Lund-Olesen · Henrik Bruus ·
Mikkel Fougt Hansen**

Abstract We present two new types of microfluidic passive magnetic bead separator systems as well as methods for performing quantitative characterizations of them. Both systems consist of a microfluidic channel with long rectangular magnetic elements of permalloy that are placed by the sides of the channel and magnetized by an external magnetic field. In one of the systems, a staggered herringbone microfluidic mixer is integrated in the channel. The characterization of the systems includes magnetic measurements of the capture-and-release efficiencies, estimates of distributions of captured beads in a channel from micrographs, and simulations and analytical models of bead trajectories, capture efficiencies, and capture distributions. We show that the efficiencies of both systems compare favorably to those in the literature. For the studied geometries, the mixer is demonstrated to increase the bead capture-and-release efficiency for a fixed flow rate by up to a factor of two. Moreover, high capture efficiencies can be achieved in the system with mixer at up to ten times higher flow rates than in the system without mixer.

Keywords Magnetic beads · Magnetic separation ·
Microfluidic · Bioseparation · Lab on a chip

Introduction

Separation of biological species by use of magnetic beads functionalized with biological molecules is a method which is widely used in biochemical laboratories. The use of magnetic beads in microfluidic systems, however, is just emerging and is receiving growing attention (Verpoorte, 2003; Gijs, 2004; Pamme, 2006). The designs presented in the literature can be divided into active magnetic separators, which utilize on-chip electromagnetic structures (Ahn et al., 1996; Choi et al., 2001a, b, 2000; Smistrup et al., 2005a; Ramadan et al., 2006), and passive magnetic separators, which utilize on-chip structures magnetized by an external magnetic field (Deng et al., 2002; Do et al., 2004; Rida and Gijs, 2004; Smistrup et al., 2005b). The reports in the literature, summarized in Table 1, have mainly demonstrated proof-of-concept and hence the information on experimental conditions and the performance of the designs is at present limited. The lack of systematic characterization makes it difficult to compare the performance of the various designs. Such a characterization is essential for the fundamental understanding of the bead capturing process and is required for moving beyond proof-of-concept demonstrations. Moreover, systematic characterizations of the different designs will make it possible to choose an optimal design for a given application.

We present a thorough quantitative study of the bead capture in two new designs of a passive magnetic separator. The study comprises: (1) the first measurements of the bead-capture-and-release efficiencies by magnetometry, (2) estimates of the distribution of captured beads in the microfluidic channel from image analysis, (3) numerical simulations of the bead capture, and (4) the derivation and validation of a simple analytical description of the bead capture. SI-units are used throughout the paper.

The first passive magnetic separator design consists of a long straight microfluidic channel. Adjacent to the channel is placed a number of soft magnetic elements as schematically illustrated in Fig. 1(a). When a homogeneous external

T. Lund-Olesen (✉) · H. Bruus · M. F. Hansen
MIC—Department of Micro and Nanotechnology, DTU, Building
345 East, Technical University of Denmark,
DK-2800 Kongens Lyngby, Denmark
e-mail: tlo@mic.dtu.dk

Table 1 Specifications and characterization of microfluidic magnetic separators presented in the literature

Ref	Cross sec. (μm^2)	Flow rate (μL/min)	Capt. eff. (%)	Characterization
Ahn et al., 1996	100 × 90	≈ 0.5	NA	OC
Choi et al., 2001a	NA	NA	NA	OC, SC. Inductance measurements are compared to simulations to approximately deduce the number of captured beads.
Choi et al., 2000, 2001b	800 × 250	3–50	NA	OC, SC. For different electrical currents, the maximum fluid flow velocity where some beads are captured is reported.
Smistrup et al., 2005a	1500 × 50	1	≈ 89	OC, OR. The capture efficiency is evaluated using simulations but not verified experimentally.
Deng et al., 2002	150 × 50	2	> 95	OC, OR. The capture efficiency is measured by counting the number of beads exiting the system before and after bead release. Difficulties releasing all beads.
Do et al., 2004	2000 × 70	3–7	NA	OC.
Rida and Gijs, 2004	200 × 200	6	NA	OC, OR. Not characterized as a magnetic separator but the ability to retain a plug of magnetic beads is characterized thoroughly up to ≈ 50 μL/min
Ramadan et al., 2006	5000 × 100	10–120	70–0	OC. The capture efficiency is evaluated by counting beads in known volumes collected at the inlet and outlet.
Present work	400 × 80 mix	10–60	100–89	OC, OR, SC, CE. The capture efficiency is evaluated using
	400 × 80	10–60	93–49	simulations (numbers in this table) and compared to measurements of
	200 × 80 mix	10–40	100–97	capture-and-release efficiencies at several flow rates. Investigation of
	200 × 80	10–40	96–74	amount of beads getting stuck in setup for different flow rates.

The following abbreviations are used: OC: Optical verification of bead capture; OR: Optical verification of bead release; SC: All beads can be removed in a system cleaning step; CE: Study of capture-and-release efficiency.
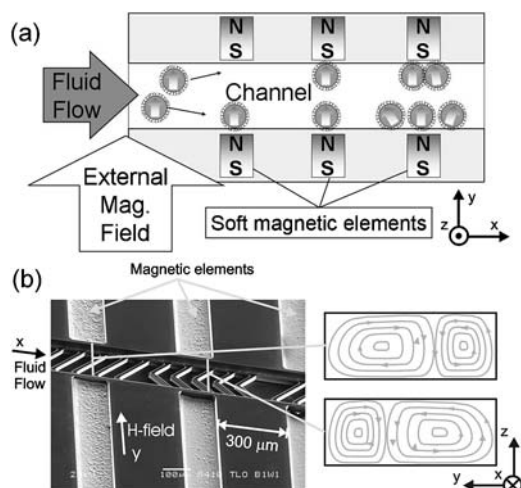

Fig. 1 (a) Sketch of magnetic separator principle. (b) Scanning electron micrograph of a section of a system with integrated microfluidic mixer (ridges at the bottom of the channel). The liquid flow in the channel is along the *x*-direction. The homogeneous external magnetic field is applied in the *y*-direction. On the right is sketched the transverse liquid velocity at the indicated channel cross-sections

magnetic field is applied along the elements, they are magnetized. This creates local maxima of the magnetic field at the channel sidewalls to which the magnetic beads are attracted and captured. When the external magnetic field is removed, the magnetic elements demagnetize, and the beads are released.

The second passive magnetic separator design is similar to the first one, but a staggered herringbone microfluidic mixer (Stroock et al., 2002a) is integrated in the channel. The principle is illustrated in Fig. 1(b). The mixer consists of ridges that extend up from the bottom of the channel. When liquid is flowing in the channel, the liquid near the ridges will tend to flow along them towards the channel sidewalls and recirculate along the channel circumference thus creating a helical flow as illustrated in the insets of Fig. 1(b). The transverse convection induced by the mixer has two consequences: (1) the beads from the central part of the channel are brought closer to the elements where the capturing force is large and (2) the beads are released more easily as they are brought away from the channel wall, where the liquid velocity is low. This presents a novel solution to the general issues in magnetic separation that the magnetic force decays rapidly with the distance from the magnetic structures and that beads captured on a wall generally are released slowly in pressure-driven systems without transverse convection.

The quantitative study of the two designs has been carried out for two different channel widths at a number of liquid flow rates. It is demonstrated that both types of systems are efficient compared to the literature, but also that the capture efficiency is enhanced by up to a factor of two in the studied systems with integrated mixer structures for a fixed flow rate. Moreover, high capture efficiencies can be achieved in the system with mixer at up to ten times higher flow

rates than in the system without mixer. The enhancement will be even larger for wider channels and provides a way to efficiently capture magnetic beads in channels with larger cross-sections. Furthermore, it is demonstrated that the beads are released faster and more reliably in the systems with mixer structures.

The distribution of captured beads along the fluidic channel is studied for both types of systems and is found to follow a power law in the systems without mixers and an exponential decay in the systems with mixers. This is in accordance with simulations and simple analytical models. To our knowledge the present work is the first quantitative study of capture-and-release efficiencies and the distribution of captured beads in a microfluidic system for a range of flow rates. The resulting fundamental understanding of the bead capture in these systems will make it possible to compare to other designs and for a user to choose an optimal design for a given application.

Design and simulations

Microsystem design

The principle of the magnetic separator is schematically illustrated in Fig. 1(a). Figure 1(b) shows a scanning electron micrograph of a system with integrated staggered herringbone mixer structures at the bottom of the fluidic channel. We define a coordinate system as indicated in Fig. 1(b) with x along the channel ($x = 0$ and $x = l$ at the inlet and outlet, respectively), y along the magnetic elements ($y = 0$ and $y = w$ at the right and left channel wall, respectively) and z along the height of the channel ($z = 0$ and $z = h$ at the bottom and top, respectively). The straight microfluidic channel has a width w of either 200 μm or 400 μm and $l \times h = 13500 \times 80 \ \mu\text{m}^2$. On each side of the channel are placed 30 permalloy magnetic elements of size $l_e \times w_e \times h_e = 4300 \times 150 \times 50 \ \mu\text{m}^3$ separated 20 μm from the channel. These elements are numbered from 1 to 30 starting at the channel inlet. The element period along the channel is $\Delta x = 450 \ \mu$m. Each herringbone consists of a wide and a narrow ridge angled in a vertex of $\pm 45°$. The ridges are 30 μm high and 21 μm wide. The herringbones are spaced 60 μm apart in groups of five. The position of the vertex alternates between left and right from one group to the next. Some of the systems have been fabricated with two fluidic inlets to enable comparisons between liquid flow simulations and experiments.

Liquid flow simulations

3D simulations of the liquid flow were used to optimize the mixer geometry for maximum transverse convection. The primary function of the mixer is to bring magnetic beads close to the sidewalls. Thus an effective mixer for bead capturing will have large transverse velocities near the sidewalls. The simulations were performed using FEMLAB 3.1 (http://www.comsol.com).

The flow is in the Stokes regime and hence the reduced steady-state equation solved for the liquid flow is:

$$\nabla p = \eta \nabla^2 \mathbf{v} \tag{1}$$

where p is the pressure, $\mathbf{v}$ is the liquid velocity, and η is the dynamic viscosity. Furthermore the liquid is assumed to be incompressible and the no-slip boundary condition is used on the channel walls. During optimization of the mixer geometry, the problem was reduced by use of periodic boundary conditions and by ignoring the fact that the wide and narrow part of the ridge switch sides for every five ridges. Thus, the parameters varied in the optimization were the channel dimensions and the width, height, period, and shape of the ridge.

The mixer is used to bring the magnetic beads close to the magnetic structures by introducing transverse components to the liquid velocities. To evaluate the efficiency of the mixer, surfaces were drawn 10 μm from the sidewalls of the channel. The average value of $|v_y|$ on these surfaces is proportional to the liquid flux in and out of the planes and can be used as a measure of the liquid exchange rate near the walls. The magnitude of the liquid rolls can also be evaluated in other ways. In the literature, the angle of the liquid velocity with respect to the channel axis just below the top surface has been used (Stroock et al., 2002b). We compared the two methods and generally found that the optimizations led to the same results.

A number of design rules for maximizing the tranverse velocity magnitude emerged from the numerous simulations: (a) The most important factor is the ridge height. Higher ridges relative to the channel height result in larger transverse velocities. However, high ridges increase the hydraulic resistance even more than the transverse velocities and introduce significant flow barriers in the channel that increase the risk of blockage. Hence, a compromise should be found for the ridge height. (b) The channel width should be at least two and preferably three to four times the channel height. (c) The ridge width should be chosen as narrow as possible. (d) When the above parameters are chosen, the ridge period should be optimized. Figure 2 shows an example where the average $|v_y|$ through two planes is extracted for a series of simulations in which the ridge period is varied. The figure shows that an optimum period exists. It also shows that the transverse velocities are larger for the wide part of the ridge than for the narrow part. This effect increases with increasing asymmetry of the system.
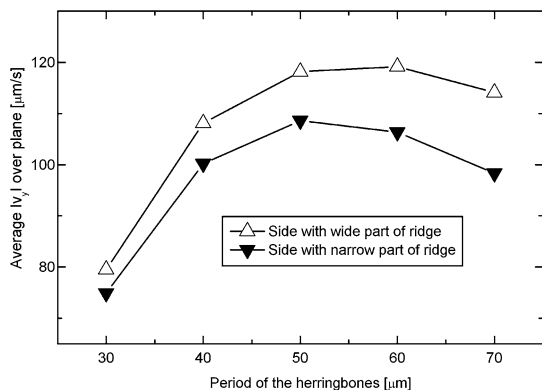
Fig. 2 Magnitude of the tranverse liquid velocities created in the channel near the sidewall as a function of the ridge period. The channel dimensions are $w \times h = 100 \times 50 \ \mu\text{m}^2$. The narrow part of the ridge occupies 40% of the channel width

For simulations of particle trajectories the flow calculations were performed with ten ridges (one full period) using periodic boundary conditions. For comparisons to flow experiments, the calculations were carried out with 30 ridges (three full periods) without periodic boundary conditions.

Magnetic field calculations

As there are no free electrical currents in the system, the magnetic field **H** from the magnetic elements can be calculated using the magnetic scalar potential φ as $\mathbf{H} = -\nabla\varphi$. The magnetic scalar potential fulfills

$$\nabla \cdot (-\mu_r \mu_0 \nabla\varphi) = 0 \qquad (2)$$

where μ_0 is the permeability of free space and μ_r is the field-dependent relative permeability. This differential equation was solved in 3D in FEMLAB 3.1 using the non-linear magnetic properties of permalloy. The calculations were carried out in a homogeneous external magnetic field of $\mu_0 \mathbf{H}_{\text{ext}} = 50$ mT introduced at the boundaries of the simulation domain by the Neumann condition

$$\mathbf{n} \cdot (\mu_r \mu_0 \nabla\varphi) = \mu_0 \mathbf{H}_{\text{ext}}. \qquad (3)$$

In the calculations, symmetry and antisymmetry planes were utilized to reduce the size of the simulation domain.

Bead trajectories and capture efficiencies

In the systems, the magnetic beads are affected by three forces: a magnetic force, a bouyancy force, and a liquid drag force. The latter is assumed to be the Stokes drag. The nth magnetic element is centered at $x_n = (n - 1/2)\Delta x$. The beads enter the channel at $(x, y, z) = (0, y_i, z_i)$. The perturbation of the liquid flow by the moving magnetic beads and interactions between beads have been neglected to make the simulations feasible. Also, the small bead mass makes the acceleration fast compared to other time scales such that the acceleration term in the equation of motion can be neglected. The bead velocity is then described by a first order differential equation, which depends only on the bead position $\mathbf{r}_b = (x_b, y_b, z_b)$

$$\frac{d\mathbf{r}_b}{dt} = \mathbf{v}_{\text{fluid}}(\mathbf{r}_b) + (6\pi\eta R_b)^{-1}[\mathbf{F}_{\text{mag}}(\mathbf{r}_b) - V_b(\rho_b - \rho_{\text{fluid}})\hat{\mathbf{z}}], \qquad (4)$$

where ρ's denote mass densities, R_b is the bead radius and V_b is the bead volume. The magnetic force, $\mathbf{F}_{\text{mag}}$, is

$$\mathbf{F}_{\text{mag}}(\mathbf{r}_b) \approx \mu_0 V_b (\mathbf{M}_b[\mathbf{H}_0(\mathbf{r}_b)] \cdot \nabla)\mathbf{H}_0(\mathbf{r}_b), \qquad (5)$$

where $\mathbf{M}_b$ is the field-dependent bead magnetization and $\mathbf{H}_0$ is the magnetic field in the absence of magnetic beads (Engel and Friedrichs, 2002). To carry out the bead trajectory simulations, the calculated liquid flow field and magnetic field were exported to tables that were subsequenly used for the numerical integration of Eq. (4). The trajectories were simulated for a large number of beads with initial coordinates on a regular grid in the channel cross section at $x = 0$. The amount of beads entering the channel at each initial coordinate was set proportional to the liquid velocity at that point. From the trajectories was found the amount of beads captured at each element along the channel in addition to the amount of beads escaping the channel. This resulted in simulated distributions of captured beads along the channel and estimates of the capture efficiency.

Approximate analytical models for the bead capture profile

System without mixer

To simplify the analytical calculations, they are carried out in the xy-plane and the z-position is taken to be the vertical centre of the magnetic elements ($z \approx 25 \ \mu$m). Furthermore, the velocity towards the channel sidewalls, dy_b/dt, due to the magnetic field from the elements is averaged along the channel (the x-direction). The extracted variation of the y-velocity with $0 \leq y \leq w/2$, where w is the channel width, was found to be well approximated by

$$\frac{dy_b}{dt} = -\beta(y_b + y_{b,\text{ref}})^{-\alpha}, \qquad (6)$$

where $\beta = 2.60 \times 10^{-18}$ ms^{-1}, $y_{b,\text{ref}}$ [m] $= 1.00 \times 10^{-4}$, and $\alpha = 3.75$ are fitting constants. The analytical calculations are further simplified by assuming a constant liquid velocity, v_x, in the channel. Using that $dy_b/dt = v_x dy_b/dx_b$ and the initial condition $(x_b, y_b) = (0, y_i)$, the solution to Eq. (6) is

$$y_b(x) = \left[(y_i + y_{b,\text{ref}})^{\alpha+1} - \beta(\alpha + 1)v_x^{-1}x\right]^{1/(\alpha+1)} - y_{b,\text{ref}}. \tag{7}$$

Given that the beads entering at $(0, y_i)$ are captured at $(x_b, y_b) = (x_c, 0)$, the relation between y_i and x_c becomes

$$y_i(x_c) = \left[y_{b,\text{ref}}^{\alpha+1} + \beta(\alpha + 1)v_x^{-1}x_c\right]^{1/(\alpha+1)} - y_{b,\text{ref}}. \tag{8}$$

The beads that are captured at the nth element are those which enter the channel with values of y_i between $y_i(x_n - \Delta x/2)$ and $y_i(x_n + \Delta x/2)$. Defining $y_n = y_i(x_n + \Delta x/2)$, the relative amount f_n of beads collected at the nth magnetic element is therefore $f_n = 2(y_n - y_{n-1})w \approx (dy_i/dx_c)_{x=x_n}(2\Delta x/w)$, i.e.

$$f_n \approx 2\Delta x \beta(w v_x)^{-1}\left[y_{b,\text{ref}}^{\alpha+1} + \beta(\alpha + 1)v_x^{-1}x_n\right]^{-\alpha/(\alpha+1)}. \tag{9}$$

Thus, for larger x, the bead capture profile is expected to follow a power law with the exponent $-\alpha/(\alpha + 1)$. If $y_n \geq w/2$ for an available n, all beads are captured at the previous elements.

System with mixer

The mixer is assumed to introduce instantaneous mixing when $x = n \cdot \Delta x$ ($n \geq 1$) and no mixing in between these values. Furthermore, it is assumed that each set of magnetic elements captures the fraction f_0 of the beads remaining in the channel after the previous set of elements. Obviously, f_0 is a function of the flow rate. Denoting the number of beads left in the channel after the nth set of elements N_n, we have

$$N_{n-1} - N_n = f_0 N_{n-1} \quad (n \geq 1), \tag{10}$$

where N_0 is the total number of beads entering the channel. From this it is seen that

$$N_n = N_0(1 - f_0)^n, \tag{11}$$

and hence that the capture efficiency of a system with n sets of elements is $1 - (1 - f_0)^n$. The fraction of beads captured at the nth set of elements is

$$f_n = f_0(1 - f_0)^{n-1}. \tag{12}$$

Hence, if Eq. (12) is fulfilled, f_n will depend exponentially on n and a plot of $\log(f_n)$ vs. n will yield a straight line with a slope equal to $\log(1 - f_0) \approx -f_0$. Equation (12) can also be written as

$$\frac{\log(f_n) - \log[f_0((1 - f_0)]}{\log(1 - f_0)} = n. \tag{13}$$

Thus, a plot of the left hand side of Eq. (13) vs. n for all flow rates using the value of f_0 determined for each flow rate should yield a straight line with slope $= 1$.

The simple model derived for the system without mixer predicts that

$$f_0 = 2y_1/w, \tag{14}$$

with $y_1 \equiv y_i(x_1 + \Delta x/2) = y_i(\Delta x)$ given by Eq. (8), because each set of elements capture all beads with a distance less than y_1 from the channel wall.

Experimental

Microsystem fabrication

The fabrication procedure uses etched structures in a silicon wafer as a mould for electroplating of magnetic structures. This method was pioneered by Wu et al. (2004) and further developed by Smistrup et al. (2006).

The fabrication procedure is schematically illustrated in Fig. 3. The starting wafers are single side polished silicon wafers on which a 1.1 μm thick oxide is grown. In (1) a 1.5 μm thick layer of AZ5214 positive photoresist (Hoechst, NJ, USA) is spun onto the wafer and patterned using UV-lithography. The wafer is hardbaked in an oven at 120°C for 25 min. In (2) the photoresist is used as oxide etch mask in buffered hydrofluoric acid (BHF) and subsequently stripped in acetone. In (3) a 6.2 μm thick layer of AZ4562 positive photoresist (Hoechst, NJ, USA) is spun onto the wafer and patterned using UV-lithography. In (4) a 30 μm deep reactive ion etch (DRIE) is performed, followed by resist strip in acetone. In (5) a 50 μm DRIE is performed, followed by oxide strip in BHF. This finishes the etched structures. In (6) an RCA clean is performed and 0.12 μm oxide is grown on the wafer for electrical insulation. In (7) 5 nm Ti and 200 nm Au is E-beam evaporated onto the wafer.

The sidewalls formed in the DRIE are almost vertical and the E-beam evaporation is designed to have poor step coverage. Therefore there is little or no electrical contact between the metal deposited in the bottom of the etched structure, and that deposited on top of the wafer. Short etches of Au in Entreat 100 (Engelhard, NJ, USA) are performed until no electrical contact is present between top and bottom of the
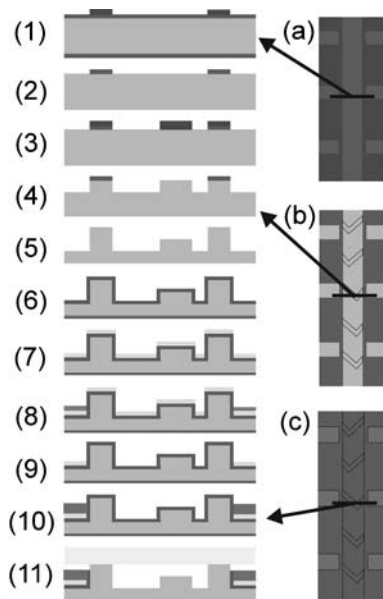
Fig. 3 Schematic fabrication sequence. (1)–(11) Cross section of part of a system. (a)–(c) Top view of part of a system. (1) Oxide grown and photo resist deposited and patterned. (2) Oxide etched in BHF and resist stripped in acetone. (3) Photo resist etch mask deposited and patterned. (4) Deep reactive ion etch (DRIE) performed and resist stripped in acetone. (5) DRIE performed and oxide stripped in BHF. (6) Oxide grown for electrical insulation. (7) Ti/Au seed layer deposited. (8) Thin Cu layer electroplated. (9) Exposed Au stripped in Entreat 100 and Cu stripped in nitric acid. (10) Permalloy electroplated. (11) Exposed insulating oxide stripped in BHF. Pyrex wafer bonded anodically to the system

etched structures. In (8) 2.5 μm Cu is electroplated onto the wafer. Since no electrical contact is present between top and bottom of the etched structures, the Cu will only be electroplated onto the conduction paths and the structures etched for the magnetic elements. The conduction paths go to the rim of the wafer where electrical contact is made. Hence, Cu will not be electroplated in the microfluidic channel. In (9) the exposed Au is stripped in Entreat 100 followed by a Cu strip in nitric acid. This leaves an oxide covered silicon wafer with Au only in the bottom of the etched structures designated for conducting paths and magnetic elements. In (10) 50 μm permalloy ($Ni_{80}Fe_{20}$) is electroplated onto the wafer forming the magnetic elements. The oxide is stripped in BHF leaving a clean top Si surface ready for anodic bonding to a pyrex wafer as seen in (11). Then the wafer is diced and inlet holes to the microfluidic channel are drilled through the pyrex lid using a diamond drill.

Experimental setup

Figure 4 shows a schematic of the experimental setup. The chip was mounted in a machined polycarbonate holder with O-ring seals. Teflon tubes with an inner diameter of 0.8 mm were connected to the holder using fittings (Minstac 062, The
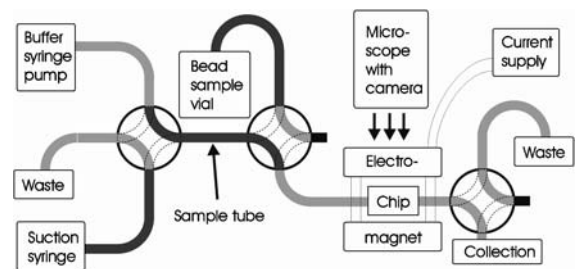

Fig. 4 Schematic of the fluidic setup. A syringe is used to suck sample from the bead sample vial into the sample tube. When the two switch valves are rotated 90°, a welldefined bead solution volume is isolated (indicated by the dark color), which can be driven into the chip by the flow from a syringe with buffer

Lee Company, CT, USA). The fluid handling was controlled using three switch valves (V-101D, Upchurch Scientific, WA, USA), two of which were used to isolate a reproducible sample volume. Care was taken to reduce dead volumes. The flow was controlled using a syringe pump. Homogeneous magnetic flux densities between 0 and 50 mT were supplied by a table-top electromagnet. Micrographs were taken in a Leica MZFLIII stereo microscope using a Sony DFW-X710 digital camera. Fluorescence micrographs were taken using FITC filters.

Experimental conditions

Magnetic beads

All experiments were carried out using a solution of My-One Streptavidin magnetic beads (Dynal, Norway) diluted with milli-Q water to a concentration of $\approx 2 \times 10^7$ beads/mL (20 μg/mL). The beads have an average diameter of 1.05 μm, a density of 1.7 g/cm^3 and a low-field magnetic volume susceptibility of 1.4. The beads were fluorescence labeled by functionalization with a DNA oligo with a FITC-label in one end and biotin at the other. The buffer used in the experiments was phosphate buffered saline (PBS) with 1% sodium dodecyl sulfate (SDS).

Flow characterization experiments

The liquid flow investigations were performed using systems with two inlets. A solution of albumin, bovine-FITC in milli-Q water was introduced through one inlet and milli-Q water through the other at a flow rate ratio of 3:10. This was carried out for a range of total flow rates between 8 and 4000 μL/min

Bead capture-and-release experiments

Bead capture-and-release experiments were carried out in the setup illustrated in Fig. 4 as follows: (1) The bead solution was sucked from the bead sample vial into the sample tube

using a syringe. (2) The two switch valves were rotated 90° isolating a well-defined sample volume of 110 μL in the sample tube and valves. (3) The electromagnet and buffer syringe pump were turned on and the sample was pushed into the system by 500 μL of buffer at a constant flow rate varying from 10 to 60 μL/min in the experiments. (4) Then, the buffer flow rate was increased to 40 to 60 μL/min to flush beads out of the tubes and valves. This ensured that no further beads were released from the fluidic setup during the release of the beads captured in the microsystem. (5) After flushing for 4–5 min the electromagnet was turned off and the beads were released. Samples were collected in 0.25 mL thin-walled plastic tubes (two for systems with mixer and three for systems without mixer) for further investigation.

It was found that beads tended to get stuck in the fluidic setup (Fig. 4) before entering the system. Therefore, series of measurements were carried out in which the samples were collected at the chip inlet as a function of flow rate. For each run, three plastic tubes with a total volume of 750 μL were collected and pooled. A similar series was carried out in which the samples were allowed to flow through the chip in zero applied magnetic field. The resulting samples were used to investigate where beads got stuck in the experiments and to quantify the amount of beads reaching and entering the microsystem. These samples are referred to as reference samples.

After each experiment, the liquid flow rate was raised to ≈ 2–5 mL/min by manually driving the flow using a syringe to clean the fluidic setup and the chip from remaining beads.

Method for quantification of bead amounts

Measurements of the saturation magnetic moment using a vibrating sample magnetometer (VSM) were used for quantifying the bead amounts (Lund-Olesen et al., 2006). A measurement was performed as follows: (1) The bead solution collected in a thin walled plastic tube was placed on top of a permanent magnet. (2) After the beads were collected at the bottom of the tube the supernatant was removed. (3) After drying, the beads were fixed at the bottom of the tube using glue. (4) The tube was mounted in a custom-made sample holder in the VSM. (5) A hysteresis curve was measured and corrected for background contributions and yielded the saturation magnetic moment of the beads, which is proportional to the number of beads. The main uncertainties in the measurements arise from sample positioning and background contributions from dust settling on the sample tube. Therefore great care was taken during the sample positioning and handling.

Measurements on known bead solution volumes between 0 and 200 μL were carried out repeatedly and a linear relation with zero offset between the magnetic moment and the bead solution volume was verified (Lund-Olesen et al., 2006). It

was estimated that the meaurements have an uncertainty of ≈ 2 nAm^2 corresponding to an initial bead solution volume of ≈ 3 μL. Thus, the method can be used to reliably quantify the amounts of beads used in the experiments.

Results and discussion

Flow characterization

The flow experiments using dyed water and buffer confirmed that the flow was laminar and in the Stokes regime for the flow rates used in the experiments. Figure 5 shows a comparison of a micrograph from an experiment and a plot from the corresponding simulation. The two are in good agreement and at least qualitatively validates the flow simulations.

Qualitative bead capture and release

Micrographs from the experiments show that the distribution of captured beads in the system with mixer differs significantly from that in the system without mixer. As an example we will discuss the micrographs shown in Fig. 6 from experiments with a flow rate of 20 μL/min and systems with 400 μm wide channels.

In the system with mixer, the amount of beads captured at the first element is high and then gradually drops element by element. After element number 18 no captured beads
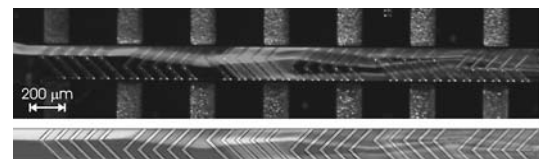

Fig. 5 Top: Fluorescence micrograph from a flow experiment in a system with two inlets. Bottom: Grayscale plot from the corresponding liquid flow simulation
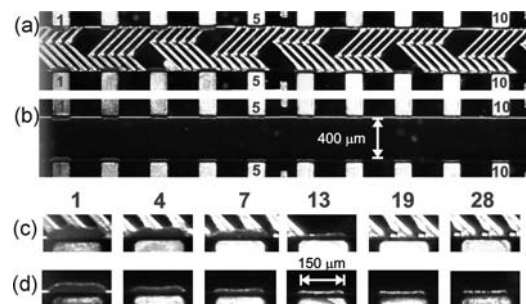

Fig. 6 (a) and (b) Overview of beads captured at the first elements (element numbers indicated) in a system with and without mixer, respectively, for a flow rate of $Q = 20$ μL/min. The beads are seen as the gray areas in the channel close to the magnetic elements. (c) and (d) Close-ups of beads captured at the indicated element numbers in a system with and without mixer, respectively
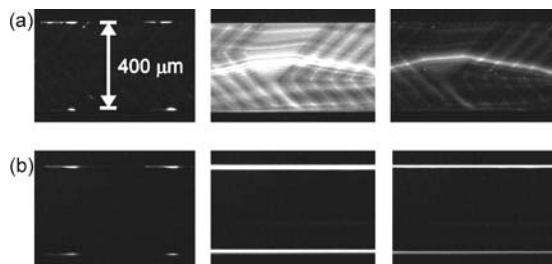
Fig. 7 Fluorescence micrographs of elements 28 to 29 (out of 30) during bead release after the magnetic field is switched off at time $t = 0$ s. The channels are 400 μm wide. (a) System with mixer at $t = 0$ s, $t = 1$ s, and $t = 2$ s. (b) System without mixer at $t = 0$ s, $t = 2$ s, and $t = 4$ s. The bright areas in all micrographs are the fluorescence signals from magnetic beads

are observed and no beads were seen escaping the channel during experiments.

In the system without mixer many beads are captured at the first element. At the following elements, the amount of captured beads rapidly drops before ending up at an almost constant but nonzero level. Magnetic beads were seen escaping the channel during experiments.

Figure 7 shows fluorescence micrographs of the release of fluorescence labeled magnetic beads upon switching off the field at time $t = 0$. In the mixer system, it is seen that the beads are quickly forced into the central part of the liquid flow and carried away. After 1 s the fluorescence signal is at maximum and after 2 s almost all beads have left the system. In the system without a mixer, the beads remain near the channel sidewalls where the liquid velocity is small and are thus released very slowly. After 2 s the fluorescence signal reaches maximum and then slowly decreases. As a result, a much larger liquid volume must be collected to obtain all the released beads. Furthermore, as the beads remain near the wall where the liquid velocity is small there is a larger tendency for the beads to settle in the fluidic setup at the system outlet where the tube diameter is large.

Bead capture and release efficiency

System cleaning

The cleaning procedure carried out after each experiment was verified by performing an experiment with fluorescently labeled beads followed by an experiment with unlabeled beads. No cross-contamination between experiments was observed.

Reference samples

The samples were collected as described in the experimental conditions section. The amount of beads collected in each run was quantified using the VSM as described in the experimental section. Figure 8 shows the measured magnetic
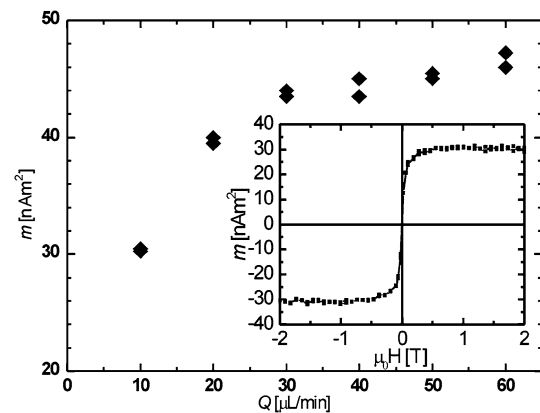

Fig. 8 Measured saturation magnetic moment, m, of collected reference samples as a function of flow rate, Q. The inset shows a typical hysteresis curve used for the determination of the saturation magnetic moment

moments as a function of the liquid flow rate. The inset in the figure shows a typical example of a measured hysteresis loop. It is clearly seen that the amount of beads reaching the system depends significantly on the liquid flow rate. Experiments where samples have been collected before and after passing through the chip and chip holder, respectively, gave within the uncertainty identical results. Hence, the reduced amount of beads collected at lower flow rates is due to beads settling in the fluidic setup prior to the chip. This setup has comparably large cross-sections and the liquid velocity is therefore small leading to gravitational settling of the beads. This also explains why the effect is more pronounced for small flow rates. The starting point for determining the capture efficiency is the amount of beads that actually reach the inlet of the chip. This amount has been shown to be reproducible in repeated experiments. We will therefore use the data in Fig. 8 as a reference corresponding to 100% capture efficiency.

Capture-and-release samples

The samples collected during capture-and-release experiments were measured in the VSM, and the signals relative to those from the corresponding reference samples defined the capture-and-release efficiencies. Figure 9 shows the measured efficiencies together with those obtained in the simulations. Although there is a considerable uncertainty in the measurements, it is clear that the experiments and simulations show the same overall behaviour. The mixer significantly increases the efficiency of the magnetic separator and the effect of the mixer becomes more pronounced as the channel becomes wider. For the 400 μm wide systems, the simulation results have been shifted –5% for the system with mixer and –12% for the system without mixer to fit the experimental data. This is probably due to beads sticking in the
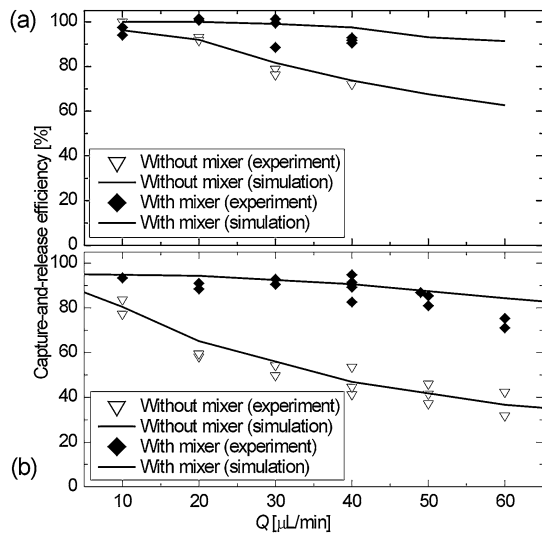
Fig. 9 Capture-and-release efficiencies in percent as function of the flow rate, Q. (a) Systems with 400 μm wide channels. The simulation results have been shifted −5% for the system with mixer and −12% for the system without mixer to adjust them to the experiments. (b) Systems with 200 μm wide channels. The simulation results have no free parameters in this graph

system and the setup after bead release and due to difficulties collecting all released beads for the system without mixer as discussed above under bead release. The effect is less pronounced for the 200 μm wide system, where the general liquid velocity in the microchannel is higher.

Distribution of captured beads

Fluorescence micrographs of the captured beads were used for further quantitative characterisation of the systems. The area of the beads captured at each element was estimated from micrographs similar to the close-ups in Fig. 6 and used as a measure of the amount of beads. In the simulations, the amount of beads captured at each element was registered. The amount of beads captured at a given element number is defined as the sum of the amounts captured at the two sides of the channel. Figure 10 shows the results from experiments and the corresponding simulations in systems with and without mixer at a flow rate of 20 μL/min. It is seen that the distributions of captured beads are similar although the area is an approximate measure of the amount of beads, which is difficult to estimate for small amounts of beads.

System without mixer

The simple analytical analysis yields that the fraction of beads captured at the nth set of elements weighted by the liquid flow rate (i.e., $f_n v_x$) can be written as a function depending only on the system geometry and the position of the
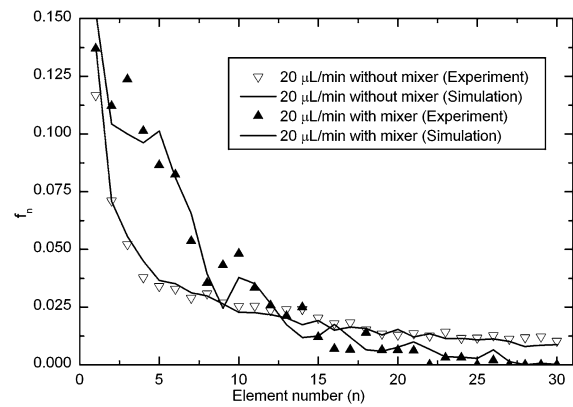

Fig. 10 Fraction of beads captured at each magnetic element for simulations of the trajectories of 4000 beads for a flow rate of $Q = 20\ \mu$L/min in 400 μm wide channels. The scaled experimental data are shown as points

nth set of elements normalized by the liquid flow rate (i.e., x_n/v_x). The latter is the time that it takes for the bead to reach the nth element. Hence, a plot of $f_n v_x$ as a function of x_n/v_x for various flow rates should fall onto a universal curve which is approximately given by Eq. (9). Figure 11 shows this scaling plot of the experimental data along with the predictions from the simple analytical analysis. Note that the predictions are without free parameters. As expected, the experiments fall onto a universal curve, which is fairly well predicted by the simple analytical model. This analysis shows that the distribution of captured beads along the channel follows a power law and that the time a bead at a given starting position is interacting with a magnetic element determines whether it is captured or not independent of the flow rate. It is noted that the deviation between the simple model and the experimental data is largest for small values of x_n, i.e., for small element numbers. This difference can be due to several effects. In
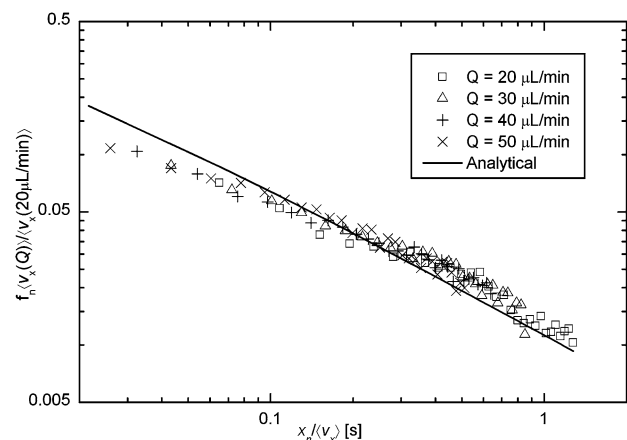

Fig. 11 Fraction of beads captured at each element scaled with $\langle v_x(Q)\rangle/\langle v_x(20\ \mu$L/min$)\rangle$ as a function of $x_n\langle v_x\rangle$ for a system without mixer and a 400 μm wide channel. The points show experimental data for four different flow rates, Q, and the line shows the analytical prediction Eq. (9)

the experiments, the comparatively large amount of beads captured at the first elements modify the liquid flow and the outermost beads are also torn loose more easily by the liquid drag. This is not taken into account in the simple model and the simulations. Furthermore, in the simple model, the liquid flow velocity was assumed to be constant across the channel. While this assumption is justified in the central part of the channel, it is not valid near the channel side wall, which is relevant for the capture of the beads on the first elements. The simulations, where the liquid velocity profile is taken into account, show a better agreement with the experimental data (shown for 20 μL/min in Fig. 10).

The bead capture efficiency predicted by the simple analytical model for the studied systems is $2y_{30}/w$ if $y_{30} < w/2$ and 1 if $y_{30} > w/2$. An evaluation of Eq. (8) for the studied flow rates yields a variation consistent with that obtained in the simulations and the measured bead capture-and-release efficiencies. The absolute value, however, is overestimated by approximately 20% compared to the experimental values for the reasons given above and in the *Capture-and-release samples* section.

System with mixer

In Fig. 10, the amount of beads captured at a given set of elements is seen to fluctuate both in the experiments and in the simulations. The reason for this is that the mixer has a different period than the elements. Hence, the liquid exchange and influx of magnetic beads varies for different elements. It is noted that the oscillations in the simulations and the experimental data occur at approximately the same positions and also that the simple analytical model does not take these fluctuations into account as it only predicts the average behavior. The experimental data points obtained for each flow rate were on average found to follow Eq. (11) and hence a value of f_0 could meaningfully be extracted for each flow rate. A corresponding analysis was carried out for the simulations. Figure 12 shows a scaling plot of all experimental data according to Eq. (13) as explained in the theory section. It is seen that the points in the scaling plot are scattered around the expected line with no systematic deviation. This shows that the average behavior can be described by the simple model presented in Eqs. (10)–(13) and hence follows an exponential decay. The scatter is mainly due to the aforementioned oscillations. There is a small offset in the vertical axis in Fig. 12, which most likely arises from an uncertainty on the absolute scaling of the obtained values of f_n.

The values of f_0 from the experiments and those predicted from simulations and the simple analytical expression Eq. (14) are shown in the inset in Fig. 12. The values of f_0 obtained from the simulations are in fair agreement with those obtained experimentally, whereas those obtained from the simple analytical expression Eq. (14) systemati-
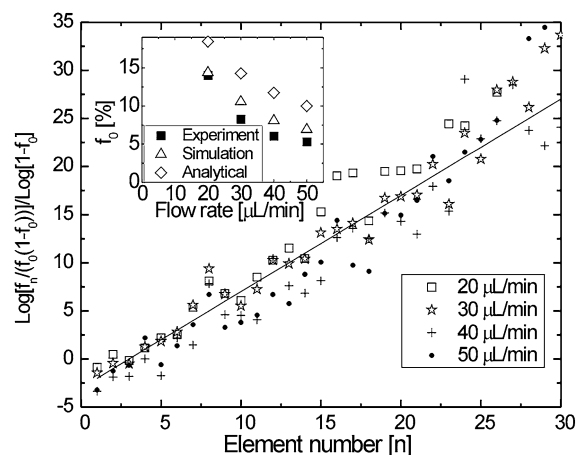

Fig. 12 Scaling plot according to Eq. (13) for a system with mixer and a 400 μm wide channel where values from all experiments have been plotted. The line is a guideline with a slope of 1. The inset shows the values of f_0 extracted from the experiments and the simulations as well as those predicted by the simple analytical model, Eq. (14)

cally overestimate the amount of captured beads. This is in agreement with the observation for the first elements in the system without mixer and the explanation is again that this model is too simplified to account for the first magnetic element.

The bead capture efficiency predicted from the simple mixer model, Eqs. (10)–(13), for the studied systems is $1-(1-f_0)^{30}$. The bead capture efficiency vs. flow rate predicted from the values of f_0 obtained from the image analysis and those obtained from the simulations are consistent with the measured capture-and-release efficiencies.

Conclusion

We have fabricated and characterized passive magnetic separators with and without an integrated staggered herringbone mixer. Both systems have simple fabrication sequences.

The capture and release of magnetic beads in the systems have been throroughly characterized experimentally and analyzed in simulations and simple analytical models. Magnetic measurements have for the first time been used to quantify the bead capture-and-release efficiency in four systems for a number of flow rates. The quantitative analysis takes into account beads settling in the fluidic setup prior to the microsystem. The quantitative characterization shows that all systems efficiently capture beads compared to those in the literature. Moreover, the integration of mixer structures significantly increases the bead capture-and-release efficiency in microfluidic systems. For a 400 μm wide channel with mixer, for example, a bead capture-and-release efficiency larger than 70–80% can be maintained at 5–10 times higher flow rates than in the system without mixer.

Fluorescence micrographs taken during bead release demonstrate that the mixer structures also facilitate the release of the beads as the liquid convection brings the beads into the central liquid flow as opposed to flowing near the channel wall.

The distribution of captured beads along the channel has been characterized experimentally from micrographs for the two types of systems. It can be approximated by a power law in the systems without mixer and an exponential decay in the system with mixer.

The capture of magnetic beads has been analyzed through simulations of bead trajectories. The simulations agree well with the experimental observations and seem able to account for the bead distribution and capture efficiency for various experimental conditions.

Simple analytical models have been developed for the bead capture. These seem to describe the essential physics of the bead capture in the two systems. However, the simple analytical analysis tends to overestimate the amount of beads captured at the first elements. The variation of the bead capture efficiencies predicted from the models agree well with with those observed in the bead capture-and-release experiments.

Although the quantification of the experimental observations, the simulations and the analytical models all involve approximations, they show very similar results and the models seem able to predict and explain the experimental observations. In addition to a fundamental understanding of the bead capture, the analytical models provide the simple means to evaluate the bead capture efficiency for various designs and experimental conditions such that an optimal design can be chosen for a given application. Currently, it is difficult to expand the comparison to other designs in the literature beyond Table 1 due to lack of corresponding data for those.

References

C.H. Ahn, M.G. Allen, W. Trimmer, Y.-N. Jun, and S. Erramilli, J. Microelectromech. Syst. **5**, 151 (1996).

J.-W. Choi, C.H. Ahn, S. Bhansali, and H.T. Henderson, Sensors Actuators B **68**, 34 (2000).

J.-W. Choi, T.M. Liakopoulos, and C.H. Ahn, Biosen. and Bioelec. **16**, 409 (2001a).

J.-W. Choi, K.W. Oh, A.H.N. Okulan, C.A. Wijayawardhana, C. Lannes, S. Bhanshali, K.T. Schlueter, W.R. Heinemann, H.B. Halsall, J.H. Nevin, A.J. Helmicki, H.T. Henderson, and C.H. Ahn, Biomed. Microdevices **3**(3), 191 (2001b).

T. Deng, M. Prentiss, and G.M. Whitesides, Appl. Phys. Lett. **80**, 461 (2002).

J. Do, J.-W. Choi, and C.H. Ahn, IEEE Trans. Magn. **40**, 3009 (2004).

A. Engel and R. Friedrichs, Am. J. Phys. **70**, 428 (2002).

M.A.M. Gijs, Microfluid. Nanofluid. **1**, 22 (2004).

T. Lund-Olesen, H. Bruus, and M.F. Hansen, In *Proc. 19th International Conference on Micro Electro Mechanical Systems (MEMS 2006)*, Istanbul (IEEE, Piscataway, New Jersey, 2006), p. 386.

N. Pamme, Lab. Chip. **6**, 24 (2006).

Q. Ramadan, V. Samper, D.P. Poenar, and C. Yu, Biosens. and Bioelectron. **21**, 1693 (2006).

A. Rida and M.A.M. Gijs, Anal. Chem. **76**, 6239 (2004).

K. Smistrup, O. Hansen, H. Bruus, and M.F. Hansen, J. Magn. and Magn. Mater. **293**, 597 (2005a).

K. Smistrup, B.G. Kjeldsen, J.L. Reimers, M. Dufva, J. Petersen, and M.F. Hansen, Lab. Chip. **5**, 1315 (2005b).

K. Smistrup, T. Lund-Olesen, P.T. Tang, and M.F. Hansen, J. Appl. Phys. **99**, 08P102 (2006).

A.D. Stroock, S.K.W. Dertinger, A. Ajdari, I. Mezic, H.A. Stone, and G.M. Whitesides, Science **295**, 647 (2002a).

A. D. Stroock, S.K. Dertinger, G.M. Whitesides, and A. Ajdari, Anal. Chem. **74**, 5306 (2002b).

E. Verpoorte, Lab. Chip. **3**, 60N (2003).

J. Wu, V. Quinn, and G.H. Bernstein, J. Micromech. Microeng. **14**, 576 (2004).